BRANCHING RATIO MEASUREMENT OF $\chi_c \to VV$

By

Osvaldo Aquines

A thesis submitted in partial fulfillment of the requirements for the degree of

MASTER OF SCIENCE

in

PHYSICS

UNIVERSITY OF PUERTO RICO
MAYAGÜEZ CAMPUS

May, 2006

Approved by:

Hector Mendez, Ph.D President, Graduate Committee	Date
Angel Lopez, Ph.D Member, Graduate Committee	Date
Eduardo Ramirez, Ph.D Member, Graduate Committee	Date
Ivette Irizarry, Ph.D Representative of Graduate Studies	Date
Hector Jimenez, Ph.D Chairperson of the Department	Date

Abstract

We report recent results on a search for exclusive hadronic decays of charmonium states (χ_{cJ}) decaying into vector-vector meson ($\chi_c \to VV$), using a sample of 3 million $\psi(2S)$ recorded with the CLEO detector. We present branching ratio measurements for $\chi_c \to VV$, which include the decays $\chi_c \to \omega\omega$ and $\chi_c \to \phi\phi$. Branching ratios for $\chi_{c1} \to \omega\omega$ and $\chi_{c1} \to \phi\phi$ are measured for the first time.

Resumen

En este análisis se reportan resultados recientes de la búsqueda de decaimentos hadronicos exclusivos de estados de charmonio (χ_{cJ}) decayendo en un par de mesones vector ($\chi_c \to VV$). Se utilizó una muestra de 3 millones de $\psi(2S)$ registrados con el detector CLEO. Se presentan las razones de producción para $\chi_c \to VV$, las cuales incluyen los decaimentos $\chi_c \to \omega\omega$ y $\chi_c \to \phi\phi$. Las razones de producción para $\chi_{c1} \to \omega\omega$ y $\chi_{c1} \to \phi\phi$ son medidas por primera vez.

To my parents.

ACKNOWLEDGMENTS

I would like to thank Peter Zweber for his intensive colaboration, Jamila Butt for helping us implement the kinematic fit, Cesar Castromonte for helping with PAW and LaTeX. Arjuna Castrillon for all his help with the solaris platform, all the Cleo 101 2005 instructors, specially Peter Onisy and of course, the Cleo Collaboration.

Also to all my friends who gave me their support during this job, It would be a long list and I don't want to leave anyone out but they know who they are and how thankful I am to them.

TABLE OF CONTENTS

LIST OF TABLES

LIST OF FIGURES

CHAPTER 1
INTRODUCTION

Since the beginning of mankind, numerous efforts have been done to classify the matter that composes nature. From the early days of Fire, Earth, Air, and Water, through the alchemist of the middle ages to the chemist of the Modern Era, this classification started to become more complex, and each time, getting to know more about the intrinsic nature of things, scientists had to deal with smaller and smaller components. For a moment, when the electrons and nucleons were discovered, people thought that was it, but afterwards it was discovered that many other tiny particles comparable to their size existed, and if it wasn't enough, it was also discovered that nucleons were made of other smaller particles called quarks. Nowadays, there are many theories that try to explain all of these elements, The Standard Model is one of the most accepted and commonly used.

1.1 The Standard Model

According to the Standard Model, everything is made out of three kinds of elementary particles and the interactions among them. All matter is made out of fundamental spin 1/2 particles called fermions (leptons and quarks) and the mediators of the forces within them, particles of spin integer called bosons.

There are six leptons, they carry integral electric charge (in units of the magnitude of the electron charge). They are divided in three generations, each one containing two members, a charged particle and its associated neutral particle called neutrino. Of this 6 leptons, each of them has its own antilepton. For example, the

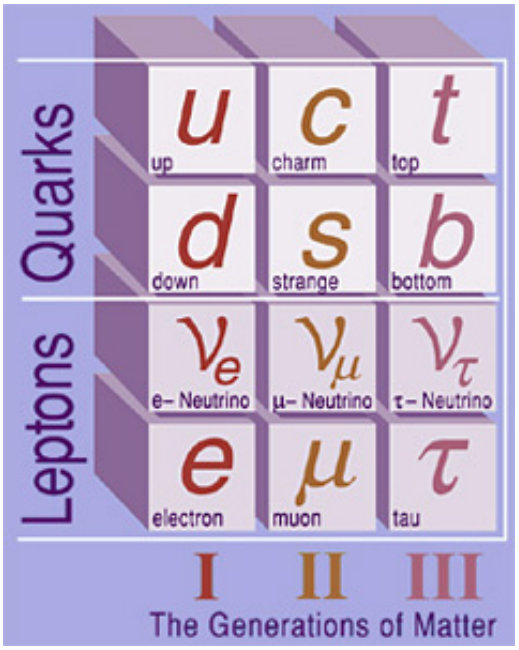

Figure 1–1: Three generations of matter

positron has the same mass of an electron but with exact opposite charge. If we count the antiparticles, we would have 12 leptons. Table 1–1 shows some of the physical properties of the leptons.

Table 1–1: Leptons (spin 1/2)

Lepton	Symbol	Charge($\|e\|$)	Mass(MeV)
electron	e	-1	0.511
electron neutrino	ν_e	0	< 0.003
muon	μ	-1	105.6
muon neutrino	ν_μ	0	< 0.19
tau	τ	-1	1784
tau neutrino	ν_τ	0	< 18.2

Similarly, quarks come in 3 generations, each one containing one positive and one negative quark. Negative quarks have a charge of Q=-$\frac{1}{3}$ and positive Q=+$\frac{2}{3}$ of the magnitude of the electron charge, each quark has a different "flavor", so we end up having six different flavors (see Table 1–2).

Table 1–2: Quarks (spin 1/2)

Flavor	Symbol	Charge($\|e\|$)	Speculative Mass(MeV)
down	d	$-\frac{1}{3}$	7.5
up	u	$+\frac{2}{3}$	4.2
strange	s	$-\frac{1}{3}$	150
charm	c	$+\frac{2}{3}$	1100
bottom	b	$-\frac{1}{3}$	4200
top	t	$+\frac{2}{3}$	174000

As for interactions there are four types known. In quantum language the different interactions are described in terms of the exchange of particles, we call these particles mediators. Mediators are particles of integral spin (bosons).

The four types of interactions are: Strong, responsible for binding quarks, and is mediated by the gluon. Electromagnetic, responsible for bound states of electrons in nuclei and the intermolecular forces in solids and liquids, the photon is the mediator of electromagnetic interactions. Weak interactions which are related to β decays and flavor changes, are mediated by the $W^{\pm}$ and the Z^0 bosons. And finally, gravitational interactions that act between any particle as long as it has mass. Gravitational interactions are by far the weakest of all, its effects are mostly seen on macroscopic physics. It is theoretically associated with a spin 2 boson called graviton which has not been found yet. Nevertheless, efforts to detect gravitons are on their way. Table 1–3 lists these mediators and some of their properties.

Table 1–3: Mediators (Bosons)

Mediator	Force	Charge($\|e\|$)	Mass(MeV)	(Spin/parity)
photon(γ)	electromagnetic	0	0	1^-
gluon(G)	strong	0	0	1^-
$W^{\pm}$	weak (charged)	± 1	81.8	1^-
Z^0	weak (neutral)	0	92.6	1^+
graviton(g) ?	gravitational	0?	0?	2^+

1.1.1 Strong Force

Quarks have many other properties besides the ones shown in Table 1–2. They also have a property called "color charge". Each quark will carry one of three colors; *red, green* or *blue*. In a similar way electromagnetics describes the interaction between electric charges, *chromodynamics*, or the laws governing the strong force, details the interactions of quarks through their "color charge". This color nomenclature is an analogy of the study of optics with the intention of being illustrative of the fact that quarks are observable only in colorless combinations. The known possibilities are combinations of two or three quarks, known as *hadrons*. *Baryons* are the three quark combinations. These must contain one of each color: red + green + blue is equal to white or colorless. *Mesons* are the quark-antiquark combinations, for instance: blue + $\overline{blue}$ = colorless. Strong force acts as a mediator to hadron daughters and electromagnetic to photon daughters.

1.1.2 Weak Force

Normally, all free hadrons (except the proton (uud)) will decay eventually into combinations of lighter hadrons, leptons and/or photons. The possible daughters in a decay depend on the force that acts as the mediator. Interactions between the forces and particles of the Standard Model can be described by the set of Vertices shown in Figure 1–2. The weak force is the only one that allows the transition of quarks to lighter quarks and leptons into lighter leptons at the vertex. In addition, the weak force explains decays that require changes in flavor for example a neutron (n) decaying to a proton (p) + electron + neutrino ν_e.

This property of the weak force implies that all stable matter in the universe is made out of only first generation of quarks and leptons. This is because the weak force not only couples within a generation but also allows for cross-generational

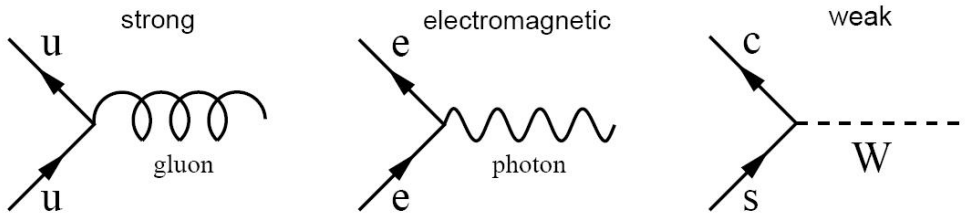

Figure 1–2: Of the three forces included in the Standard Model, only the weak force allows for quarks or leptons to change flavor and generation at the vertex.

transitions. For quarks, these couplings are summarized in the Cabbibo-Kobayashi-Maskawa (CKM) Matrix,

$$\begin{pmatrix} d' \\ s' \\ b' \end{pmatrix} = \underbrace{\begin{pmatrix} V_{ud} & V_{us} & V_{ub} \\ V_{cd} & V_{cs} & V_{cb} \\ V_{td} & V_{ts} & V_{tb} \end{pmatrix}}_{CKMmatrix} \begin{pmatrix} d \\ s \\ b \end{pmatrix}$$

In other words, the weak force does not "see" for instance a simple s quark but an s', which is a linear combination of d, s and b quarks,

$$s' = V_{cd}d + V_{cs}s + V_{cb}b. \tag{1.2}$$

The magnitude of these matrix elements $|Vij|$ is related to the quantum mechanics probability amplitude with which a quark could change of flavor, lets say an "$up-type$" quark i transition into a "$down-type$" quark j, within or even between generations. At this era, such magnitudes are not calculable from fundamental principles and must be determined experimentally. Curiously, these experimental measurements have revealed a pattern in the CKM matrix. The elements on the diagonal are approximately equal to one, which means that a quark most likely make a transition within its own generation. The matrix elements become smaller,

almost symmetrically, as the element goes off the diagonal. The actual range of each element are summarized in the following CKM matrix [1]:

$$|V_{ij}| = \begin{pmatrix} 0.9742 - 0.9757 & 0.219 - 0.226 & 0.002 - 0.005 \\ 0.219 - 0.225 & 0.9734 - 0.9749 & 0.037 - 0.043 \\ 0.004 - 0.014 & 0.035 - 0.043 & 0.9990 - 0.9993 \end{pmatrix}.$$

Based on this, interactions that involve matrix elements that lie on the diagonal are considered "Cabbibo Favored" while those that involve off-diagonal elements are told to be "Cabbibo Suppressed".

1.2 Gluons

Gluons carry colour and can interact with one another by exchanging further gluons. This behavior is very different to photons that are electrically neutral, so they don't interact among them. According to QCD there are many "colours", a particle might change its color (ex. from red to blue) by emitting a gluon - which possess the 'colour mismatch'- say purple. In QED by contrast there is only one charge and this is retained by the particle emitting an electrically neutral photon.

Because gluons carry color, the property associated with the strong interaction, a possible Feynman diagrams for these interactions where gluons interact with each other are:

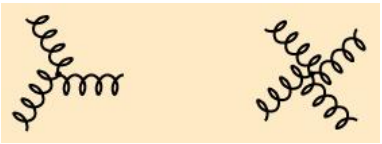

Figure 1–3: Feynman diagrams for glueballs

A theoretical particle made up entirely of gluons is called a glueball. Glueballs are color singlets and therefore can exist as free particles. However, their experimental detection is difficult since the glueballs mix with quark-antiquark states (like ordinary flavor-neutral mesons). The difficulty is therefore determining which observed mesons are glueballs and which are the usual quark-antiquark state.

1.3 Vector Mesons

Mesons with total spin 1 and odd parity (usually noted as $J^P = 1^-$) are called Vector Mesons (see Table 1–5). In particular, some vector mesons like rho ($\rho^+\rho^-\rho^0$), omega (ω) , phi (ϕ), rho prime (ρ'), J/psi(J/ψ), psi-primes ($\psi(2S), \psi''$) and upsilon (Υ) have neither strangeness nor charm quantum number. These are important to the electromagnetic behavior of hadrons because their neutral members have the same spin, intrinsic parity and charge conjunction as the photon ($J^{PC} = 1^{--}$) (see Table 1–4). As a result, the photon can transform virtually into one of the neutral vector mesons before interacting with a hadron. This possibility is the basis of the vector dominance model [2]. Unlike baryons that in any reaction the creation of one baryon aways is always accompanied by the creation of an antibaryon because the total baryon number is absolutely conserved. This is not the case for the creation of vector mesons because they do not carry baryon number. Table 1–4 shows a partial list of vector mesons.

Table 1–4: Partial list of vector mesons

Particle observed	I^G	J^P	Mass (MeV/c^2)	Lifetime (sec)	Dominant decay mode	Strangeness
$\rho^+\rho^-\rho^0$	1^+	1^-	770	4×10^{-24}	$\pi\pi$	0
ω	0^-	1^-	782	7×10^{-23}	$\pi^+\pi^-\pi^0$	0
ϕ	0^-	1^-	1020	2×10^{-22}	K^+K^-	0

Table 1–5: Quark assignment of vector mesons

Meson	Quark Content	Charge($\|e\|$)
ρ	$u\bar{d}$, $d\bar{u}$, $(u\bar{u} - d\bar{d})/\sqrt{2}$	+1,-1,0
K^*	$u\bar{s}$, $s\bar{u}$,$d\bar{s}$,$s\bar{d}$	+1,-1,0,0
ω	$(u\bar{u} - d\bar{d})/\sqrt{2}$	0
ϕ	$s\bar{s}$	0
J/ψ	$c\bar{c}$	0
D^*	$c\bar{d}$,$d\bar{c}$,$c\bar{u}$,$u\bar{c}$	+1,-1,0,0
Υ	$b\bar{b}$	0

1.4 Charmonium

The charm quark was proposed in 1970 by Glashow, Ilioupous, and Maiani, and its experimental discovery was achieved in 1974 when two groups using two different techniques observed a narrow e^+e^- resonance at 3.1 GeV. The first group was Ting et al, at Brookhaven National Laboratory (BNL) using two magnetic spectrometers to detect the e^+e^- pair resulting from proton collisions in a Berylium target [2]:

$$p + Be \rightarrow e^+e^- + anything. \tag{1.3}$$

The sharp peak in the e^+e^- invariant mass (see Figure 1–4) was an evidence of the production of a new particle that subsequently decayed into an e^+e^- pair. The particle was named J by this group.

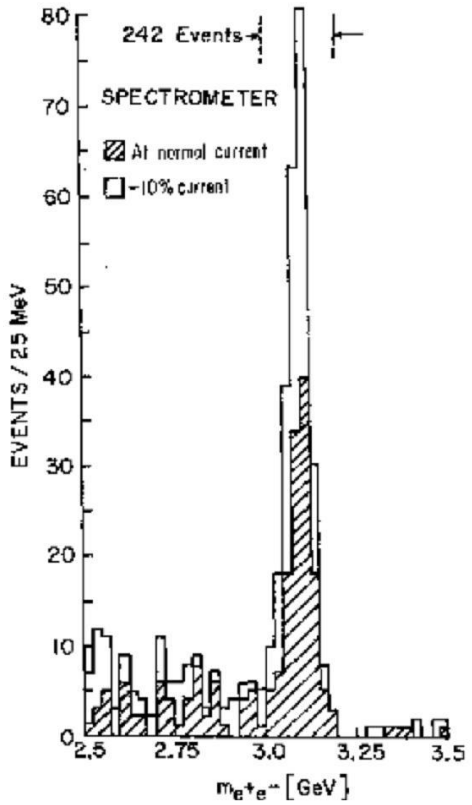

Figure 1–4: Mass spectrum showing the existence of J.

The same particle was independently discovered at the Stanford Linear Accelerator (SLAC) e^+e^- storage ring by a collaboration of SLAC and the Lawrence Berkeley Laboratory. They named this particle ψ, nowadays this particle is called J/ψ. Later on they found its excited states $\psi(2S)$ and ψ''.

Nowadays it is well known that the J/Ψ is the lowest mass $c\bar{c}$ system with the same quantum numbers as photons, that explains why it is produced more than any of the other members of its system. The $c\bar{c}$ bound states were named charmonium in analogy to positronium, whose bound level structure was similar.

There are excited $c\bar{c}$ states: Singlet S states called η_c's and Triplet S states are ψ's and triplet P states (spin 0,1,2) named χ_{c0}, χ_{c1} and χ_{c2}.

The spectra of $c\bar{c}$ [3] as far as it is known today, is shown on Table 1–6 and Figure 1–5:

Table 1–6: Properties of charmonia

Meson	J^{PC}	Mass(GeV)
η_c	0^{-+}	2.980
J/ψ	1^{--}	3.097
χ_{c0}	0^{++}	3.415
χ_{c1}	1^{++}	3.511
χ_{c2}	2^{++}	3.556
h_c	1^{+-}	3.594
$\eta_c(2S)$	0^{-+}	3.594
ψ'	1^{--}	3.686

Compared with J/ψ and $\psi(2S)$ decays, one has much less knowledge on PC $= ++$ χ_{cJ} decays.

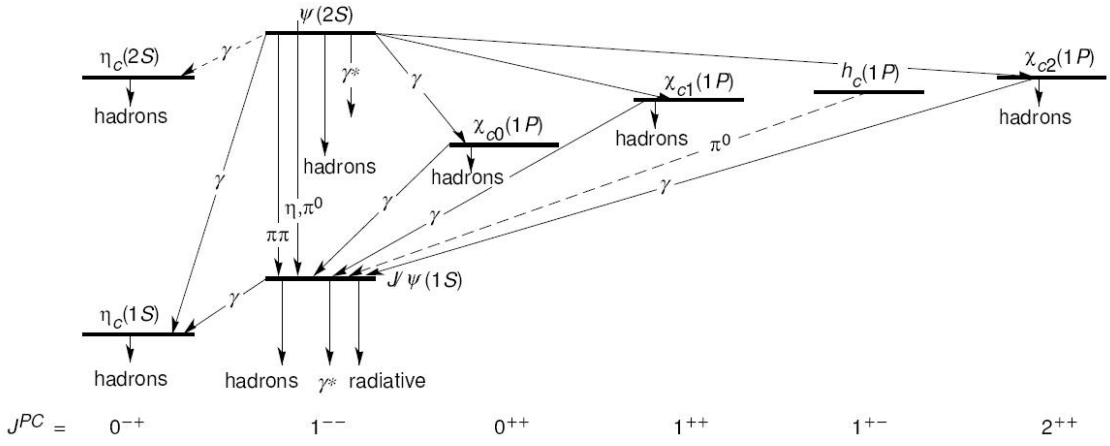

Figure 1–5: Spectrum and transitions of the charmonium family

CHAPTER 2
OBJECTIVES AND PREVIOUS WORK

2.1 Justification

In comparison with J/ψ and $\psi(2S)$ decays, one has much less knowledge on PC = ++ χ_{cJ} decays. The decays $\chi_c \to VV$, where V is a vector meson, provide a direct window on glueball dynamics in the 0^{++}, 1^{++} and 2^{++} channels since they may proceed via $c\bar{c} \to$ gg $\to q\bar{q}q\bar{q}$ (see Fig. 2–1).

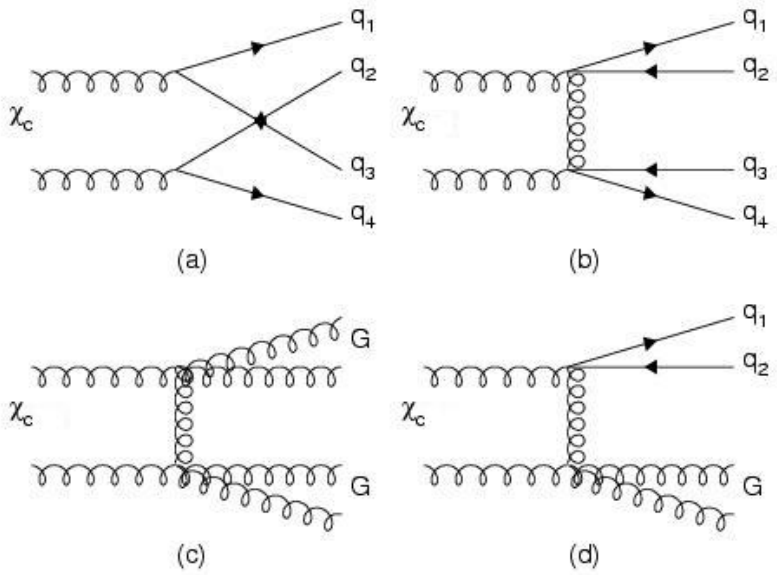

Figure 2–1: Schematic pictures for the decays of χ_{cJ} into meson pairs via the production of different components.

To explain these decays via gg, Qiang Zhao [4], in recent work, presents a factorization scheme taking into account OZI-rule violations and SU(3) flavour symmetry

breakings. The purpose of his work is to disentangle the roles played the OZI-rule violations and SU(3) flavour symmetry breakings, which will correlate with the final state meson wavefunctions in χ_c decays. A better precision on these measurements will improve this glueball dynamics model.

2.2 Objectives

The objective of this work is to measure the branching ratios of the $\chi_c \to VV$, where V represents a vector meson ω or ϕ. This measurement is done for each of the three χ_c's (χ_{c0}, χ_{c1} and χ_{c2}) states decaying to $\chi_c \to \phi\phi$ and $\chi_c \to \omega\omega$. Based on CLEO-c detector resolution, it is expected that this work will improve the precision on existing measurements of χ_c two body light vector meson decays.

As seen in Table 1–6, the invariant masses of χ_{c0}, χ_{c1} and χ_{c2} are 3.415, 3.511 and 3.556 GeV respectively. The small difference between χ_{c1} and χ_{c2} invariant masses (45 MeV) has made it difficult for other experiments with less resolution to separate these channels, in fact as mentioned before, these channels have not been separated previously and so the branching ratios of χ_{c1} remain unknown.

2.3 Previous Work

Previous measurements of $\chi_c \to VV$ using these channels have been done by the Beijing Spectrometer (BES) Collaboration [5] [6] by using a sample of 14 million $\psi(2S)$'s. Their results are shown on Tables 2–1, 2–2 and Figures 2–2(a), 2–2(b) were as follows:

Table 2–1: BES Branching ratios and relevant numbers

Quantity	$\chi_{c0} \to \omega\omega$	$\chi_{c1} \to \omega\omega$	$\chi_{c2} \to \omega\omega$
Number of Events	38.1 $\pm$9.6	—	7.4
Efficiency (%)	1.66	—	1.55
BR($\chi_c \to \omega\omega$)$\times 10^{-3}$	2.29 $\pm$0.58 $\pm$ 0.41	—	1.77 $\pm$0.47 $\pm$ 0.36

As is noticeable, they were only able to measure $\chi_{c0} \to \omega\omega$, $\chi_{c2} \to \omega\omega$, $\chi_{c0} \to \phi\phi$ and $\chi_{c2} \to \phi\phi$, so the intention of this work is to take advantage of the CLEO-c detector resolution and measure the three χ_{cJ} states.

Table 2–2: BES $\chi_c \to \phi\phi$ Branching ratios and relevant numbers

Quantity	$\chi_{c0} \to \phi\phi$	$\chi_{c1} \to \phi\phi$	$\chi_{c2} \to \phi\phi$
Number of Events	7.6 $\pm$2.8	—	13.6 $\pm$3.7
BR($\chi_c \to \phi\phi$)$\times 10^{-3}$	0.92 $\pm$0.34 $\pm$ 0.38	—	2.00 $\pm$0.55 $\pm$ 0.61

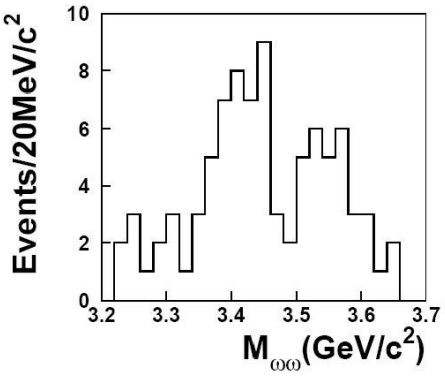

(a) BES measured signal for $\chi_c \to \omega\omega$

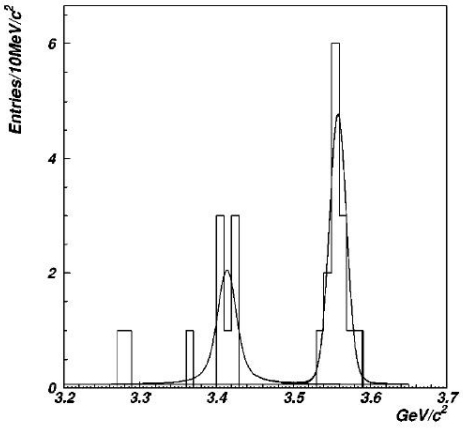

(b) BES measured signal for $\chi_c \to \phi\phi$

Figure 2–2: BES measured signals

CHAPTER 3
THE EXPERIMENT

The CLEO-c detector is in the CESR (Cornell Electron Storage Ring) which is an accelerator facility for e^+e^- collisions. The CESR is at Cornell University at Ithaca NY. CLEO-c is the sixth generation of the CLEO detector that has been used since 1979. The whole facility is known as Wilson Laboratory housed on a hillside at Cornell's Campus. CESR is a circular tunnel that has 768 meters in circumference, located 12 meters below Cornell's Alumni Fields (see Figure 3–1) .

Figure 3–1: An up view of Wilson Lab.

3.1 Cornell Electron Storage Ring CESR

The CESR receives its name (Cornell Electron Storage Ring) because it stores electrons and positrons. It is capable of producing collisions between them with

center of mass energies between 3 and 12 GeV. It is composed of three parts: the linear accelerator, the synchroton, and the storage ring. (see Figure 3–2) .

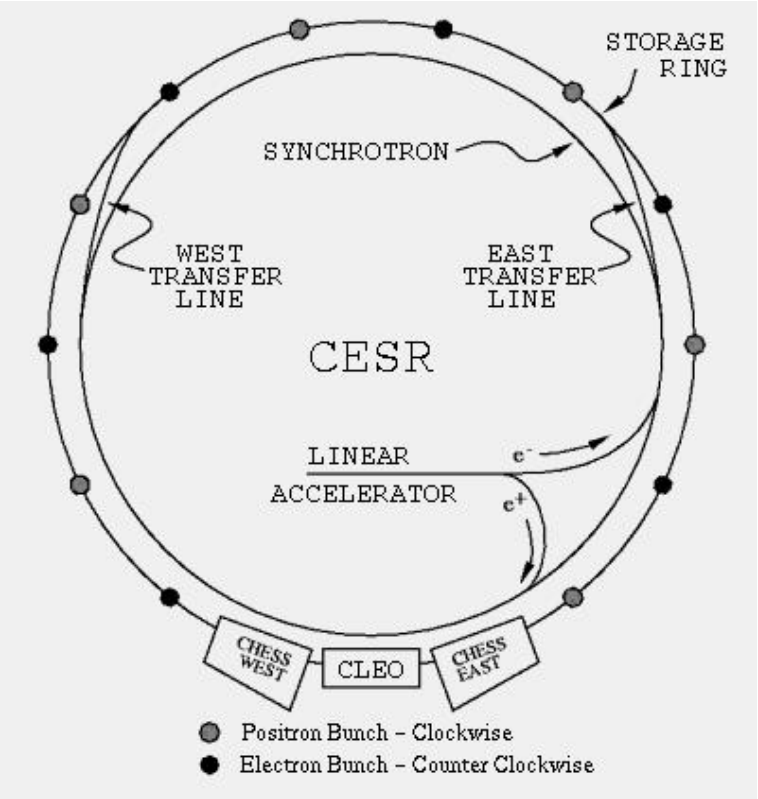

Figure 3–2: An schematic view of CESR.

3.1.1 The Linear Accelerator

The linear accelerator is located inside the CESR ring (see Figure 3–2). It is where the whole process starts. A filament is heated to obtain electrons, that are colected and compresed into packets by a prebuncher. Then, they are accelerated in a 30 meter long vacuum pipe that has many accelerating sections with syncrhonized oscillating electric fields. At the end of the linear accelerator electrons have been accelerated up to 300 MeV.

Positrons do not occur naturally in matter, so this is the reason why it is done first. An electron beam is generated and accelerated to 140 MeV and then collided on a movable tungsten plate that is located at half the length of the linear accelerator.

Showers of electrons, positrons and X-rays (Photons) emerge from the plate. The positrons are separated, focused, and acelerated in the remaining length of the linear accelerator at about 200 MeV [7].

3.1.2 The Synchroton

In separate phases, electrons and positrons coming from the linear accelerator are inyected into the synchroton. Inside it, positrons travel clockwise and electrons counterclockwise (as looking from above). The Synchroton consists of 192 3 meter long sections of bending magnets to keep the electron or positron bunches to stay in a circular path, and four 3 meter long linear accelerators placed symmetrically around the ring to constantly increase their energies. As it is expected, the more energy the particles acquire, the higher the magnitude of the magnetic field in the magnets and electric field in the cavities should be in order to keep the bunches within the circular beam pipe of the synchroton. After a bunch (either of electrons or positrons) has completed 4000 loops around the ring in just about a hundreth of a second, it reaches its maximum energy and is injected into the storage ring. The entire acceleration cycle is repeated 60 times per second for about 10 minutes until the required beam currents are built up in the storage ring.

3.1.3 The Storage Ring

The storage ring uses the same guide field principle as the synchrotron, that is that particles travel in a circular orbit in vacuum under the presence of a magnetic field. This is done the following way: particles are steered around the storage ring by a series of dipole bending magnets and focused by a series of quadrupole and sextupole magnets, with final-focusing quadrupole magnets located directly outside of the CLEO-c detector. As it is natural for a charged particle on a circular orbit, beams going around the storage ring lose energy by synchroton radiation. Such loss is recovered by using superconducting radio frequency cavities operating at a frequency of 500 MHz.

Particle bunches inside the storage ring travel around in a single 90 mm x 50 mm elliptical vacuum pipe with its major axis in the horizontal plane. Electrons and positrons are separately grouped into nine clusters called trains. Each train has up to five bunches separated by a 14 ns spacing. As it occurs positron-electron collisions at non-desirable locations could happen, but this is prevented by four electrostatic separators with electric fields in the horizontal plane pushing the orbit of the electron and positron trains around each other into so called pretzel orbits [8] (see Figure 3–3).

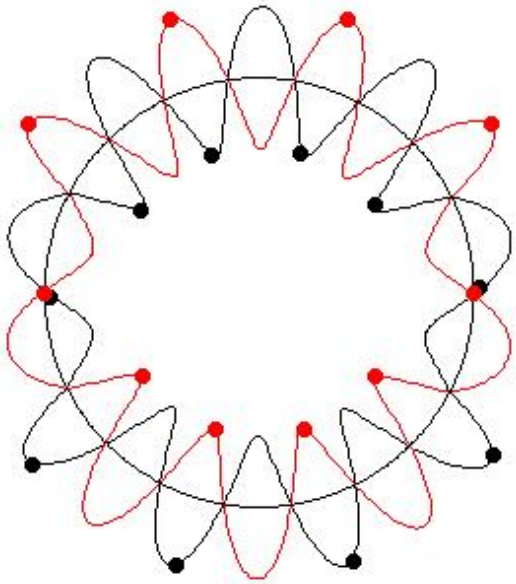

Figure 3–3: An schematic view of Pretzel Orbits.

Another interaction point potentially exists at the opposite side of the storage ring from the CLEO-c detector but the beams are separated by two vertical electrostatic separators. The effective interaction point is enclosed by the CLEO-c detector. There, the beams collide almost head-on. By this, we are taking into account the small crossing angle of 2.5 mrad into the ring. This allows for bunch by bunch collisions of the positron and electron trains.

3.2 The CLEO-c detector

As electron and positron beams collide almost in the middle point of the CLEO-c detector, they annihilate. These annihilations give birth to new particles. And such particles decay again into others and so on, until we deal with relative long-lived charged and neutral particles, that we are able to detect in our detectors. For intermediate states, we reconstruct them by means of their daughter particles.

There are five different types of detected charged particles (we also have to take into account their respective antiparticles): the electron (e) , muon (μ), pion (π), kaon (K) and proton (p). These particles leave tracks on the drift chamber, and they also deposit energy on the calorimeter, so we can now measure the momentum and energy of them and by this, we can measure their masses. Specially, muons are able to pass through the muon chambers, that is how we distinguish them from the rest of the particles. Because charged particles give us a lot of information and we can have accurate measures it is always preferable to work with them.

Of the neutral particles, the most widely used is the photon (γ). The rest of them are very difficult to observe, like the neutron (n) or the very long lived K_L^0. Neutrinos (ν) cannot be detected directly in this kind of experiment, we deal with them in terms of the missing energy of an event.

The CLEO-c detector is cylindrically symmetric, and has its axis of symmetry along the beam axis. It is almost completely hermetic and it covers 93 % of the solid angle. Its main components are: The inner drift chamber, the main drift chamber, the RICH (Ring Imaging Cherenkov) detector, the crystal calorimeter, and the muon detection chamber. With exception of the muon chamber, the rest of the components are operated within a superconducting solenoidal coil that produces a uniform 1.0 Tesla magnetic field going parallel to the axis of symmetry of the detector. The detector is shown on Figure 3–4 .

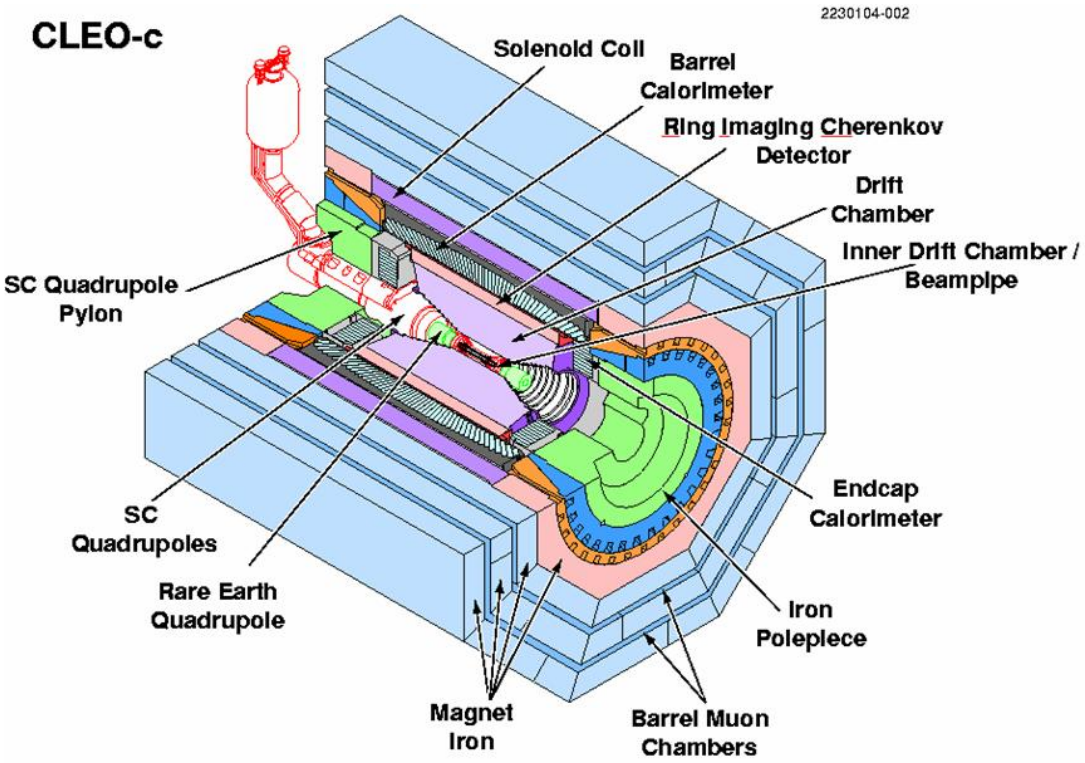

Figure 3–4: The CLEO-c detector.

3.2.1 Interaction Region

The interaction region of CLEO-c consists of a special section of the beam pipe which is the only part of it that is constructed of beryllium. As the rest of the beam pipe, beryllium is electrically conducting, but it differs in density. Its low mass is used to minimize the amount of multiple scattering of the resulting decay products as they pass out of the Interaction Region into the body of the CLEO-c detector.

The inner radius of the beam pipe in this region is 1.875 cm and is 1 mm thick. Such thickness takes into account a double wall to allow the flow of a cooling fluid along the length of the beam pipe to get rid of the heat generated by the radiation inside the Interaction Region.

3.2.2 Inner Drift Chamber

Just outside of the interaction point and beryllium part of the beam pipe, is the six-layer inner drift chamber. It can detect charged particles with $|cos\theta| < 0.93$,

where θ is the angle between the particle and the beam line where positrons come from. It consists of 300 drift cells filled with a helium-propane gas mixture. Each cell consists of a sense wire surrounded by eight field wires, forming a nearly square cell shape with a half cell size of 5 mm. Field wires are shared between neighboring cells, and neighboring layers are shifted laterally by one half cell width. A 1.9 KV difference in potential is applied to create an electric field between the sense and field wires. When a charged particle passes through a cell, it ionizes the gas. After that, free electrons are attracted toward the sense wire. The electric field near the sense wire is strong enough to cause the ionized electrons on the sense wire. The transit time of the electron pulse, together with the timing structure of the electron and positron bunches in the storage ring, is transformed into a distance of closest approach to the sense wire based on the drift velocity of the ionized electrons. A wire hit consists of a collection of ionized electrons on a sense wire; it is used to determine the trajectory of a charged particle.

The radial distance covered by the inner drift chamber is from 4.1 to 11.7 cm having an inner wall made of aluminum 1 mm thick and an outer wall made of 127 μm thick Mylar. The end plates consist of 16.5 cm machined aluminum plates located beyond the 93 % solid angle coverage. The gas inside of the inner drift chamber is a mixture of Helium and Propane having a radiation length of aproximatel 330 m. Sense wires are 20 μm in diameter, and they made of gold plated tungsten. Field wires are 110 μm diameter and made of aluminum. Wires in each layer are rotated in the ϕ direction to determine z information of the charged particle.

3.2.3 Main Drift Chamber

The Main Drift Chamber is just outside the inner drift chamber. It is the primary source of position and momentum measurements of charged particles. The radial distance covered by it is from 13.2 to 79 cm. It consists of 9795 drift cells arranged in 47 layers. The first 16 layers have their field and sense wires along

the beam axis and the remaining 31 are rotated in the ϕ direction to determine z information of the charged particle, just like the inner drift chamber. The inner wall of the main drift chamber is 2.0 mm thick expanded acrylic with 20 μm aluminum skins. Its outer wall is made of two layers of 0.8 mm thick aluminum cylindrical shells and is lined with 1 cm wide cathode rings. Wire material, gas mixture, cell geometry, end plate material, power supplies and readout electronics are the same as the inner drift chamber, with the exceptions that half the cell is 7 mm and the potential difference applied in each cell is of 2.1 KV. The radiation length of the main drift chamber is about 2%.

A parameter measured in the drift chamber that can be used for particle identification, is the energy loss. As a charged particle passes through the drift chamber, it looses energy due to ionization. The amount of energy loss per unit length (dE/dx) is related to the velocity of the particle (see Figure 3–5). To use this information as a particle ID cut, we use a χ^2 distributed variable defined as follows:

$$S_i = \left(\frac{(dE/dx)_{measured} - (dE/dx)_{expected,i}}{\sigma} \right)^2 \tag{3.1}$$

Basically, it is the measurement of the difference between the measured dE/dx value and the characteristic expected value for particle hypothesis i (i = e,μ,π,K,p) for this experiment and σ is the uncertainty in the dE/dx measurement. The drift chamber primarily measures the specific ionization for e, μ, π, K and p because these are the only common charged particles that traverse the drift chamber. Typical dE/dx resolutions are around 6%. Figure 3–5 shows how for momentum $<$ 0.5 GeV/c pions can be separated from Kaons, and for momentum $<$ 1 GeV/c, protons can be separated from kaons and pions.

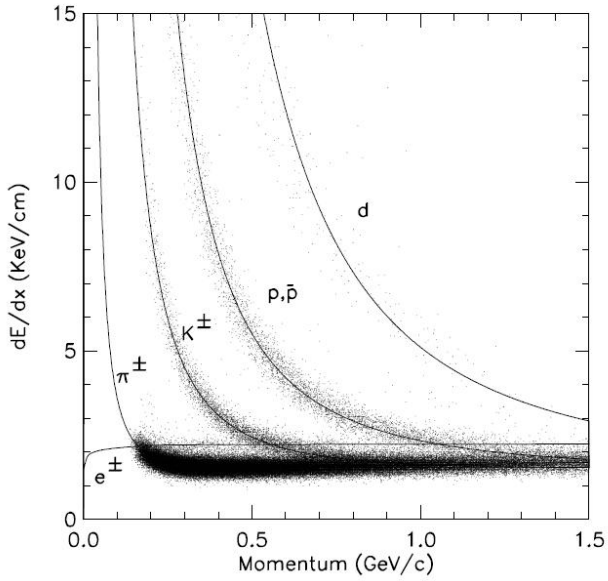

Figure 3–5: Measurement of dE/dx as a function of particle momentum

3.2.4 RICH (Ring Imaging Cherenkov)

The RICH detector (Ring Imaging Cherenkov), is just outside the main drift chamber and it covers a radial distance from 82 to 101 cm. The basic way it works is the following: If a charged particle travels in a medium at a speed greater than the speed of light in it, it emits radiation. Such radiation is called Cherenkov photons. The photons are emmited in a conic path around the particle's trajectory. The apex of the cone, or in other words, the angle that the cone makes with the trajectory of the particle, is called Cherenkov angle, and it is defined in terms of the velocity of the particle in the following way:

$$cos\Theta = \frac{1}{\beta n} \tag{3.2}$$

where β is the velocity of the particle in units of c and n is the index of refraction of the medium. Written in terms of the momentum and mass of the particle we have

$$cos\Theta = \frac{1}{n} \cdot \sqrt{1 + \frac{m^2}{p^2}} \tag{3.3}$$

So by measuring the Cherenkov angle and its momentum, we can identify the particle.

In a RICH detector, Cherenkov photons are not focused, and the Cherenkov angle is determined by allowing the photons to propagate over a finite space. That is why it is called a proximity focusing Cherenkov detector. It is composed of the following elements: a radiator material where the charged particle radiates the Cherenkov photons, an expansion volume, and photon detectors. Radiators are plates made of lithium fluoride (LiF). The expansion volume is about 16 cm thick, and it is filled with nitrogen gas. The photon detectors are higly segmented multiwire proportional chambers (MWPC) filled with a methane-triethylamine (TEA) gas behind 2 mm calcium fluoride windows [8]. Radiators cover about 83 % of the solid angle and have a radiation length of 12 % . We can observe in Figure 3–6 a one tenth view of the RICH detector in the r - ϕ plane and an example of a charged candidate charged track with its associated Cherenkov photons.

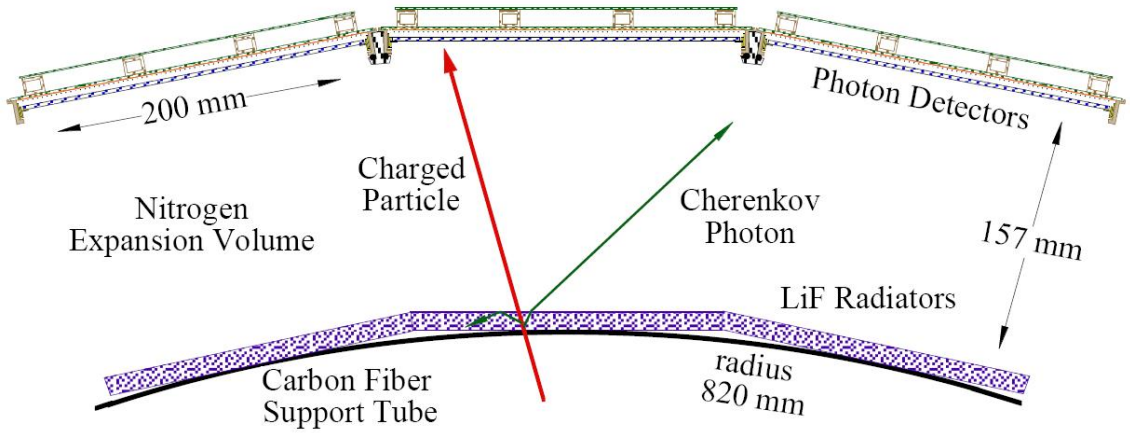

Figure 3–6: r - ϕ section of one tenth of CLEO-c RICH detector as seen from the end.

For particle identification, Cherenkov photon information is used to derive a likelihood for a particular particle hypothesis. The likelihood weigths each possible optical path traveled by a photon taking in account the length of the radiation

path and the refraction probabilities from inverse ray tracing. The logarithm of the likelihood of a particle hypothesis is χ^2 distributed, therefore the difference of two different distributions is also χ^2 distributed. So as a particle ID test we use the variable:

$$\chi_i^2 - \chi_j^2 = -2lnL_i + 2lnL_j \tag{3.4}$$

or commonly seen as

$$\chi_i^2 - \chi_j^2 = 2ln\frac{L_j}{L_i}. \tag{3.5}$$

Figure 3–7 shows how pions (π) can be separated from kaons (K) , the variable plotted is 2 ln $\frac{L_\pi}{L_K}$ for 1.0-1.5 GeV/c pions for the open points and kaons for the filled points [9] . From there we can see that if we choose such variable to be <0 or >0 we can do a fine separation between them.

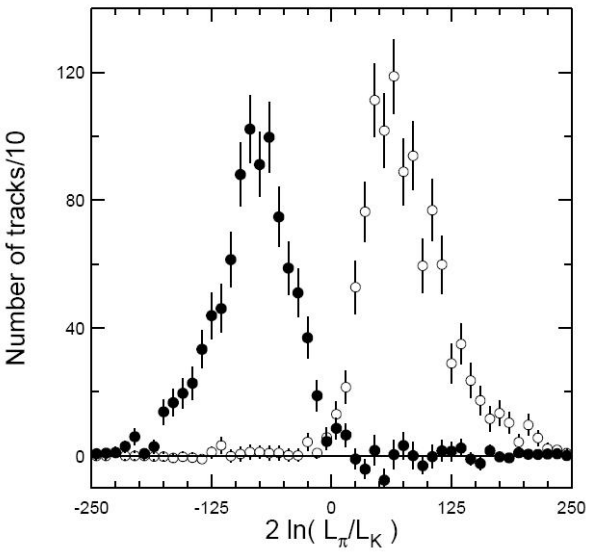

Figure 3–7: Distribution of 2 ln $\frac{L_\pi}{L_K}$

3.2.5 Crystal Calorimeter

Between the RICH detector and the superconducting solenoidal coil, we have the calorimeter. The calorimeter is made of 7781 thallium doped cesium iodide

blocks. There are three different types of reactions that can occur depending on the incident particle [8]:

If the incident particle is a photon, electron or positron, it would produce an electromagnetic shower. An electromagnetic shower consists of the following. A photon will disintegrate into an electron-positron pair, electrons and positrons will emit *bremsstrahlung* (brake radiation). So any of the three types of particle can start this process. So the process is repeated many types, this means, the bremsstrahlung photons will disintegrate into electron positron pairs and so on. This keep on going until we have a large number of low energy electrons, positrons, and photons. Low energy positrons will annihilate with electrons and produce a pair of photons, low energy photons will begin to ionize the atoms and finally, low energy electrons bind to the Thallium impurity in the crystal. As Thallium returns form the excited state, it will emit visible light. The light is detected by a silicon photo diode.

For any charged particle except electrons or positrons, the particle ionizes the atoms in the crystal, and the liberated electrons will be captured by the Thallium. That is why we call those incident particles *minimum ionizing particles*.

For incident hadrons, they interact strongly with the atomic nucleus of the crystal. By these strong interactions, a large number of neutral pions are produced. Such pions decay immediately to a pair of photons and produce electromagnetic showers. An extreme case of strong interaction would be an antiproton or an antineutron annihilation.

The photon reconstruction energy resolution is $\sigma_E/E = 1.5$ % at 5 GeV, 4% at 100 MeV and 7% at 30 MeV and the $\pi^{\mathbf{0}}$ mass resolution is in the range of 5-7 MeV/c^2 depending on photon energy and location of the shower in the calorimeter [10].

3.2.6 Muon Detector

Between the magnetic field return iron layers, there are proportional chambers for muon identification. Muons generally pass trough all the rest of the layers. They normally are the only charged particles that arrive to this point. The muon detector is a collection of alternating particle detectors and several layers of iron sheets. The purpose of the iron is to let only the most penetrating particles go trough the detectors while it also acts as a flux return for the superconducting magnet. There are three layers of plastic streamer counters at depths 36, 72 and 108 cm around the barrel. Counters have 3 layers being 8.3 cm and 5 m long. Each one contains eight 50 μm diameter silver-plated copper beryllium axially aligned node wires to provide r - ϕ measurements. Charge division can be used to extract z [1]. A charged particle detectd in the muon chamber can travel a maximum of 7.2 to 10.0 nuclear interaction lentghs depending on their flight direction.This muon detector covers 85 % of the solid angle. End caps are instrumented with only one layer of these counters .

To determine if a hit in the muon detector is associated with a charged particle track, the track is traced out from the main drift chamber and, after taking into account multiple scattering and energy loss, it is projected through the muon detector. A two-dimensional χ^2 fit is used to test if the hit can be associated with the track. The hit in the muon chamber is identified with the track if $\chi^2 < 16$ [8] .

3.3 From CLEO III to CLEO-c

CLEO-c is a reconfigured version of the CLEO III detector. CLEO-c was designed to operate at the charm resonances instead of at the Upsilon region. To carry out this goal, two main modifications were done at the accelerator and detector level. The conversion of the CESR accelerator for low energy operation required the addition of 18 meters of wiggler magnets to enhance the transverse cooling of the beam at low energies, and in the CLEO-c detector, a low mass inner drift chamber was

installed instead of the CLEO III silicon vertex detector. In addition, the solenoidal field was lowered to 1 T [10] to improve momentum resolution for charmed particle decays.

Both detector configurations are cylindrically symmetric and provide 93% coverage of the solid angle for charged and neutral particle identification. The detector component important for this analysis are the main drift chamber, the Ring Imaging Cherenkov detector and the CSI Crystal Calorimeter, all of which are common to both detector configurations. In addition, we are using in CLEO-c the inner drift chamber which adds more precision to track reconstrucction for lower momentum.

CHAPTER 4
ANALYSIS

4.1 Introduction

A $\psi(2S)$ is produced in an e^+e^- collision at the center of mass energy of $\sqrt{s}$=3.686 GeV. After a small fraction of time the $\psi(2S)$ decays into a wide range of modes. One of its decay modes is the radiative decay $\gamma + \chi_c$ which is our primary interest. Because the $\psi(2S)$ is almost at rest in the laboratory frame, the expected energy of the radiated photon is fixed and it is directly dependent of the invariant mass of the χ_c. The resolution of the CLEO-c detector for reconstructing photons, allows us to look at the energy of the radiated photon to search for χ_c, and to resolve among the three χ_{cJ} states. In our case, we are interested in VV decays, so we look for decays such as:

$$\chi_c \to \omega\omega \quad \text{and } \chi_c \to \phi\phi.$$

To accomplish this task, we reconstructed the whole event, this implies to reconstruct all the charged and neutral particles in the event. Since the event was built completely, the event must be consistent with the total center of mass beam energy, including the crossing angle of the two beams.

To identify ω and ϕ, we used the most copious modes: $\omega \to \pi^+\pi^-\pi^{\mathbf{0}}$ and $\Phi \to K^+K^-$. The $\pi^{\mathbf{0}}$' s are reconstructed via their final state $\gamma\gamma$.

The charged particles such as pions (π) and kaons (K) are reconstructed in the tracking system and are identified among each other by using the RICH detector and the energy loss (dE/dx) information from the drift chamber. Neutral particles such as γ are identified in the electromagnetic calorimeter.

The decay chain used to identify $\chi_c \to \omega\omega$ was:

$$\psi(2S) \to \gamma\chi_{cJ}\ (J = 0, 1, 2) \to \gamma\omega\omega \to \gamma\pi^+\pi^-\pi^{\mathbf{0}}\pi^+\pi^-\pi^{\mathbf{0}} \tag{4.1}$$

with $\pi^{\mathbf{0}}$'s decaying into a pair of γ's. So we end up having an event with four charged tracks and five clusters in the calorimeter (photons).

Similarly, for $\chi_c \to \phi\phi$ the decay mode is:

$$\psi(2S) \to \gamma\chi_{cJ}\ (J = 0, 1, 2) \to \gamma\phi\phi \to \gamma K^+K^-K^+K^-. \tag{4.2}$$

In these events, we end up having four charged tracks and one photon. For this reason, we expect that the reconstruction efficiency for $\chi_c \to \phi\phi$ will be greater than $\chi_c \to \omega\omega$ due to the smaller number of photons involved.

In general, the technique used in this analysis is as follows: A computer simulated MC (Monte Carlo) sample was generated to study a particular decay and measure its reconstruction efficiency. Then, after measuring the efficiency, the exact same analysis is done on the real events sample, and count the number of signal events. After extracting these numbers, we calculated the branching ratios (and their errors) the for these decay modes. A branching ratio for a decay is defined as the ratio between the decay rate of an individual decay mode with respect to the total decay rate.

The systematic error on these branching ratios shares common contributions from other recent CLEO experiment analysis, such as the number of produced $\psi(2S)$ events (3%) , luminosity (1 %), etc. So these numbers will be taken from there [11].

4.2 Data Sample and Monte Carlo Data

The data sample used in this analysis were collected at the CESR e^+e^- storage ring which has been running in the charm meson region. Our analysis is based on 3.08 million $\psi(2S)$ decays, which corresponds to a total integrated luminosity of 5.63 pb^{-1}. Approximately half of this data (2.74 pb^{-1}) were taken with the CLEO III

Table 4–1: $\psi(2S)$ Data Sample

Quantity	CLEO III	CLEO-c	Total
Dataset(s)	24-26-28	32	4 sets
Runs	129257-129488 129897-130817 131594-131640	202527-202655	
# Runs	227	105	332
$N_{\psi(2S)}$ $\times 10^6$	1.56	1.52	3.08
$\sigma_{\psi(2S)}$	3%	3%	3%
Luminosity(γ γ) (pb^{-1})	2.74	2.89	5.63
Luminosity uncertainty	3%	3%	3%
Energy Spread σ_s	1.5 MeV	2.3 MeV	

detector while the remainder (2.89 pb^{-1}) were colected with the CLEO-c detector. Table 4–1 taken from [11] summarizes the characteristics of the data sample.

Monte Carlo events were generated with EvtGen for CLEO-c. 10,000 $\psi(2S) \rightarrow \gamma\chi_c$ events (1/3 decaying to χ_{c0}, 1/3 decaying to χ_{c1} and 1/3 decaying to χ_{c2}), where $\chi_c \rightarrow \omega\omega$ and $\omega \rightarrow \pi^+\pi^-\pi^{\mathbf{0}}$ and $\pi^{\mathbf{0}} \rightarrow \gamma\gamma$. 10,000 events for $\chi_c \rightarrow \phi\phi$ and $\Phi \rightarrow K^+K^-$. For CLEO III MC events were built using QQmodel14. Similarly 10,000 events were generated for each channel. These event generators were combined with a GEANT based detector modeling [12] to simulate the full reconstruction proccess.

4.3 Event Selection

As mentioned before, we identified χ_{cJ} $(J = 0, 1, 2)$ via the final states composed by the vector-vector mesons $\chi_c \rightarrow VV$ which included the decays $\chi_c \rightarrow \omega\omega$ and $\chi_c \rightarrow \phi\phi$ where we have reconstructed $\omega \rightarrow \pi^+\pi^-\pi^{\mathbf{0}}$ and $\Phi \rightarrow K^+K^-$. $\pi^{\mathbf{0}}$ is reconstructed by $\pi^{\mathbf{0}} \rightarrow \gamma\gamma$.

Events were selected containing four or more charged tracks. Each track is required to have a polar angle θ within the fiducial region $|cos\theta| \leq 0.93$, to have

its closest distance ($d0$ along the x-y plane) to the interaction region within 5 mm ($d0 < 0.5\ mm$), and a closest distance along the beam line $z0 < 5\ cm$.

In the case of $\chi_c \rightarrow \omega\omega$, the events are required to have at least 5 photons and from such photons two $\pi^{\mathbf{0}}$'s must be reconstructed. For the other mode, we required the events to have at least 1 photon.

All photons are required to have a minimum energy of 30 MeV, not to be from noisy cells (hot showers). We consider photons either from the endcap or barrel section of the calorimeter.

A pair of photons is considered to come from a $\pi^{\mathbf{0}}$ if the reconstructed $\gamma\gamma$ mass is at most 3σ away from the $\pi^{\mathbf{0}}$ nominal mass, taking into account the detector resolution and passed the $\pi^{\mathbf{0}}$ 1-C Fit.

To identify between pions and kaons, basic RICH and dE/dx cuts were applied. A track is considered a pion if it survives a RICH cut $L\pi - Lk < 0$, otherwise it is considered to be a kaon candidate ($L\pi - Lk > 0$). A 3σ energy loss (dE/dx) cut was also applied.

For $\chi_c \rightarrow \omega\omega$, we are considering only those $\pi^+\pi^-\pi^0$ combinations that have an invariant mass consistent with the ω mass within $\pm$ 50 MeV around its nominal mass. Similarly, in the case of $\chi_c \rightarrow \phi\phi$ only those K^+K^- combinations that have an invariant mass consistent with the ϕ mass within $\pm$ 50 MeV around its nominal mass were considered.

Finally, the whole event is reconstructed and a 4-C kinematic fit is performed constraining the total four-momentum of the event to the LabNet4Momentum (4-Momentum measured in the laboratory frame, taking into account the beam crossing angle). This implies four constraints:

$$p_{xEvent} - p_{xLab} = 0$$

$$p_{yEvent} - p_{yLab} = 0$$

$$p_{zEvent} - p_{zLab} = 0$$

$$E_{Event} - E_{Lab} = 0$$

Selected events are required to have a fitted $\chi^2 < 25$. The kinematic fit identifies correctly events of our interest, when matching the tracks and showers that conform the event with the $\psi(2S)$ energy at which the beam is tunned. Only events reconstructed with 4 real tracks and 1 real photon (5 real photons for $\chi_c \to \omega\omega$) pass the fit eliminating combinations that use fake tracks and/or hot showers. This is due to the fact that fake signals are normally not consistent with the beam energy. So, the loose cut in the number of tracks and showers is justified by the accurate selection of particles. Finally, the fit improves the momentum and energy resolution of all particles selected in the event.

4.4 Data Analysis

Due to the fact that we are dealing with a radiative $\psi(2S)$ decay and in order to achieve a better resolution, we plotted the photon energy instead of the χ_c invariant mass.

The E_γ values for χ_{cJ} $(J = 0, 1, 2)$ are respectively 261, 171 and 128 MeV [13]. In order to count the number of signal events, we fitted 2 gaussian functions for the χ_{c1} and χ_{c2} and one Breit Wigner function for the χ_{c0} peak due to the fact that it has a considerable natural width. We assumed constant background.

Measurements were carried out separately for CLEO III and CLEO-c data and we calculated the final measure as the weighted average:

$$\bar{x} = w_{III} \cdot \bar{x}_{III} + w_c \cdot \bar{x}_c \tag{4.3}$$

where w_{III} and w_c are 1.56/3.08 and and 1.52/3.08 respectively. $\bar{x}_{III}$ and $\bar{x}_c$ are the measurement on each experiment.

First, the fits were made over the generated MC samples to obtain the efficiencies for each χ_c peak via the next formula:

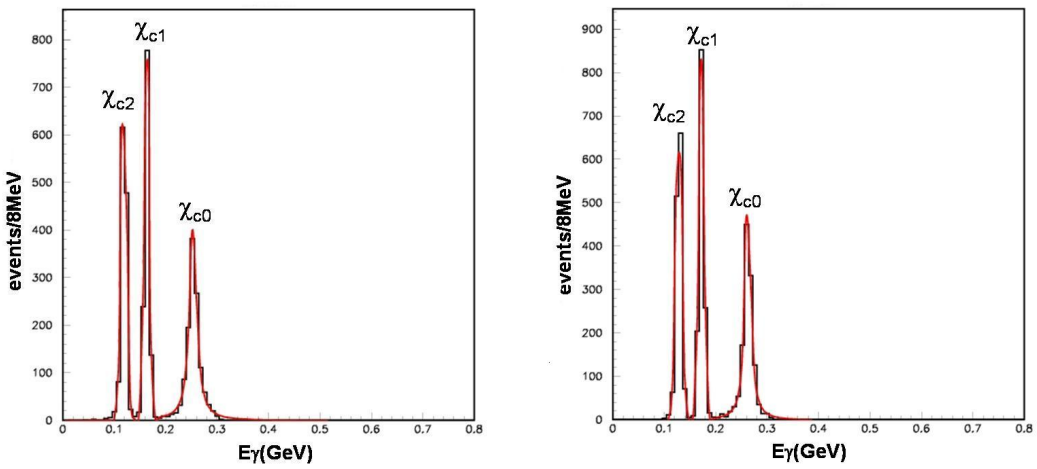

(a) $\chi_c \to \phi\phi$ sample for CLEO III MC (b) $\chi_c \to \phi\phi$ sample for CLEO-c MC

Figure 4–1: $\chi_c \to \phi\phi$ MC sample

$$\epsilon = \frac{number\ of\ reconstructed\ events}{number\ of\ generated\ events}. \tag{4.4}$$

4.4.1 Analysis for $\chi_c \to \phi\phi$

MC and Efficiencies

The Maximum Likelihood method is used to fit the photon energy spectrum shown in Figures 4–1(a), 4–1(b) and the number of MC reconstructed signal events were measured to calculate the reconstruction efficiencies (and the statistical errors) for each final state observed on CLEO III and CLEO-c (Table 4–2).

Table 4–2: $\chi_c \to \phi\phi$ Efficiencies (%)

Quantity	$\chi_{c0} \to \phi\phi$	$\chi_{c1} \to \phi\phi$	$\chi_{c2} \to \phi\phi$
CLEO III	40.2± 1.1	34.7± 1.0	36.3± 1.0
CLEO-c	41.6± 1.1	39.9± 1.1	39.9± 1.1

A comparison of these efficiencies and the weighted average for each of the χ_{cJ} states are shown in figure 4–2. Light differences show up between the efficiencies for CLEO III and CLEO-c mainly due to the improvements made to the CLEO-c detector.

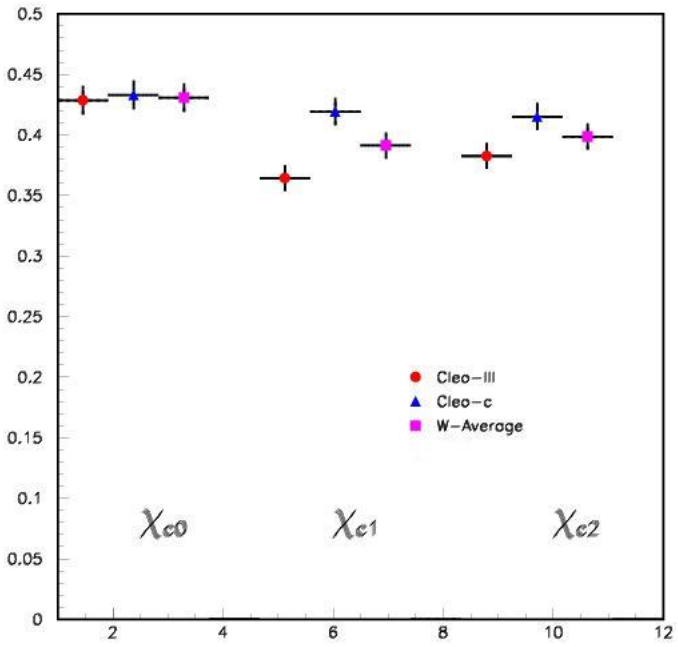

Figure 4–2: $\chi_c \to \phi\phi$ Efficiencies

Results

The number of observed data events (and the statistical errors) in CLEO III and CLEO-c (shown in Table 4–3) were measured by fitting the photon spectrum (Figures 4–3(a) and 4–3(b)) with the same functions used for the MC data (2 gaussians plus 1 Breit Wigner). Our experimental resolution made it possible to separate the χ_{c1} and χ_{c2} peaks and so, we clearly observed the three $\chi_c \to \phi\phi$ contributions.

Table 4–3: Number of $\chi_c \to \phi\phi$ Events

Quantity	$\chi_{c0} \to \phi\phi$	$\chi_{c1} \to \phi\phi$	$\chi_{c2} \to \phi\phi$
CLEO III	12.2 ± 3.6	5.8 ± 2.5	18.8 ± 4.4
CLEO-c	17.9 ± 4.5	7.9 ± 3.0	14.8 ± 4.5

Verification was done to check that the K^+K^- combinations were consistent with the ϕ mass, as can be observed in figures 4–4(a) and 4–4(b) (CLEO III and CLEO-c combined signal). Figure 4–4(a) shows K^+K^- combinations that survive

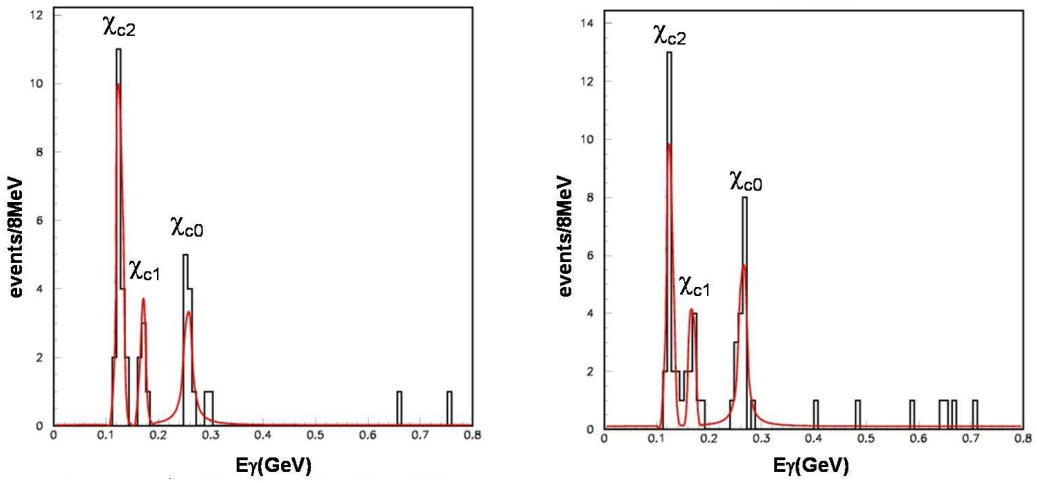

(a) $\chi_c \to \phi\phi$ sample for CLEO III data (b) $\chi_c \to \phi\phi$ sample for CLEO-c data

Figure 4–3: $\chi_c \to \phi\phi$ Data sample

all cuts. The box in 4–4(b) represents a 50 MeV boundary around the nominal mass of ϕ (1020 MeV), only events inside that box were considered.

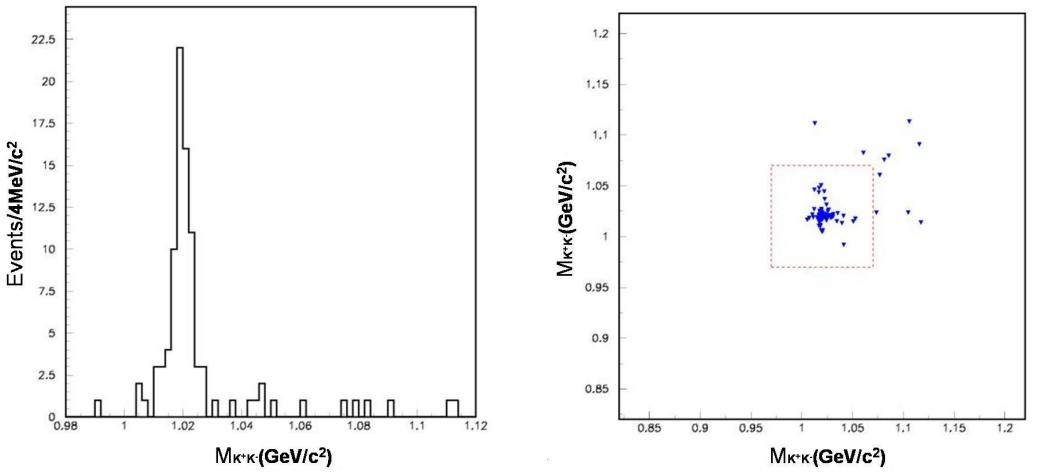

(a) K^+K^- invariant mass (b) K^+K^- vs K^+K^- invariant mass scatter plot

Figure 4–4: K^+K^- combinations

Branching ratios for each state were determined by:

$$BR(\chi_c \to \phi\phi) = \frac{N^{rec}_{\chi_c}}{N_{\psi(2S)} \cdot \epsilon} \cdot \frac{1}{BR(\psi(2S) \to \gamma\chi_c) \cdot BR(\Phi \to K^+K^-)^2} \tag{4.5}$$

where:

$N^{rec}_{\chi_c}$ is the number of reconstructed χ_c events (Table 4–3),

$N_{\psi(2S)}$ is the number of produced $\psi(2S)$ events (Table 4–1),

ϵ is the decay mode reconstruction efficiency (Table 4–2),

BR($\psi(2S) \to \gamma\chi_c$) is the branching ratio for $\psi(2S) \to \gamma\chi_c$ decay taken from recent CLEO results [14] and

BR($\Phi \to K^+K^-$) is the branching ratio for $\Phi \to K^+K^-$ decay taken from the PDG table [13].

Table 4–4 shows a summary of the final branching ratios, number of event and efficiencies for this mode. The first errors are statistical and the second are systematic.

Table 4–4: $\chi_c \to \phi\phi$ Branching ratios and relevant numbers

Quantity	$\chi_{c0} \to \phi\phi$	$\chi_{c1} \to \phi\phi$	$\chi_{c2} \to \phi\phi$
Number of Events	30.0 ± 8.2	13.8± 5.4	37.1± 8.7
Efficiency (%)	41.0 ± 1.1	37.3 ± 1.1	38.0 ± 1.1
BR($\chi_c \to \phi\phi$)($\times 10^{-3}$)	1.10 ± 0.29 ± 0.10	0.55 ± 0.21 ± 0.08	1.40 ± 0.33 ± 0.23

systematics

To study systematics, we started by doing fit variations:

- Using 3 gaussians for the fit instead of 2 gaussians plus a Breit-Wigner
- Loosing the χ^2 fit
- Changing the bin size
- Changing the fit range

For each of these variations we re-calculated all over again and measured the deviation from our central values. Our central value for each χ_c state is shown in the first point in figures 4–5(a), 4–5(b) and 4–5(c). The stability of this measurement is remarkable.

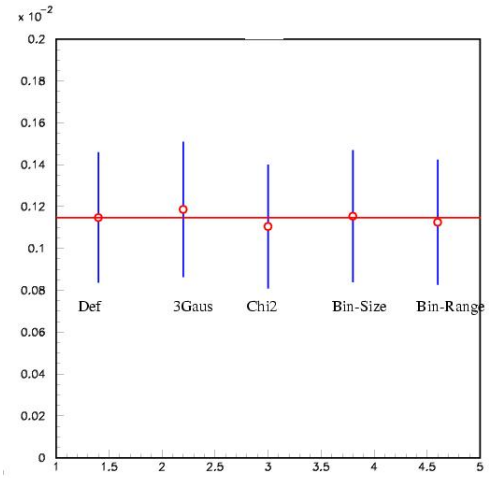

(a) $\chi_{c0} \to \phi\phi$ systematics

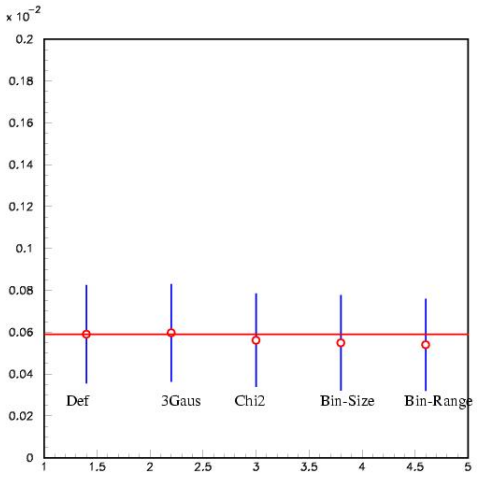

(b) $\chi_{c1} \to \phi\phi$ systematics

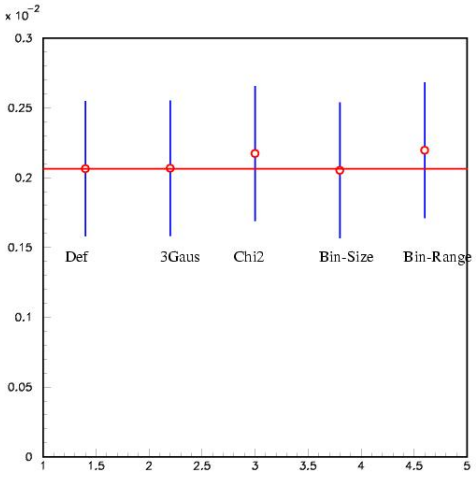

(c) $\chi_{c2} \to \phi\phi$ systematics

Figure 4–5: $\chi_c \to \phi\phi$ systematics

The systematic error including the experimental resolution and track reconstruction are common to other CLEO experiment analysis. These were taken from a more copious mode such as $J/\psi \to l^+l^-$ [11].

Systematic error due to Branching ratios of intermediate states were taken from PDG [13], except for the BR($\psi(2S) \to \gamma\chi_{cJ}$ $(J = 0, 1, 2)$) which was obtained from recent CLEO results [14].

Table 4–5 summarizes all contributions to systematic errors. The total systematic error is determined by the quadratic sum of all terms.

Table 4–5: $\chi_c \to \phi\phi$ Individual sources and total systematic error (%)

Source	$\chi_{c0} \to \phi\phi$	$\chi_{c1} \to \phi\phi$	$\chi_{c2} \to \phi\phi$
Number of $\psi(2S)$ Events	3	3	3
Luminosity	1	1	1
Using 3 Gaussians	3.4	1.1	0.1
Loosing χ^2	3.8	4.9	5.2
Reducing bin size by half	0.5	7	0.6
Four Tracks	1.6	1.6	1.6
BR($\psi(2S) \to \gamma\chi_{cJ}$ $(J = 0, 1, 2)$)	5.0	6.0	6.5
BR($\Phi \to K^+K^-$)	1.2	1.2	1.2
Total	8.3	14.1	11.2

4.4.2 Analysis for $\chi_c \to \omega\omega$

MC and Efficiencies

Similarly to $\chi_c \to \phi\phi$, The Maximum Likelihood method is used to fit the photon energy spectrum shown in Figures 4–6(a), 4–6(b) and the number of MC reconstructed signal events were measured to calculate the reconstruction efficiencies (and the statistical errors) for each final state observed on CLEO III and CLEO-c (Table 4–6).

Table 4–6: $\chi_c \to \omega\omega$ Efficiencies (%)

Quantity	$\chi_{c0} \to \omega\omega$	$\chi_{c1} \to \omega\omega$	$\chi_{c2} \to \omega\omega$
CLEO III	11.5± 0.6	10.7±0.6	11.7±0.6
CLEO-c	16.5± 0.8	14.1±0.7	14.6±0.7

A comparison of these efficiencies and the weighted average for each of the χ_{cJ} states are shown in figure 4–7. Differences between the efficiencies of CLEO III and CLEO-c are more noticeable in this case and, in general, efficiencies are smaller than $\chi_c \to \phi\phi$, due to the fact that in this we require two π^0 which lower the reconstruction efficiency. It is also noticeable that BES [5] efficiency is 10 times smaller than any of our efficiencies. (see Figure 4–7).

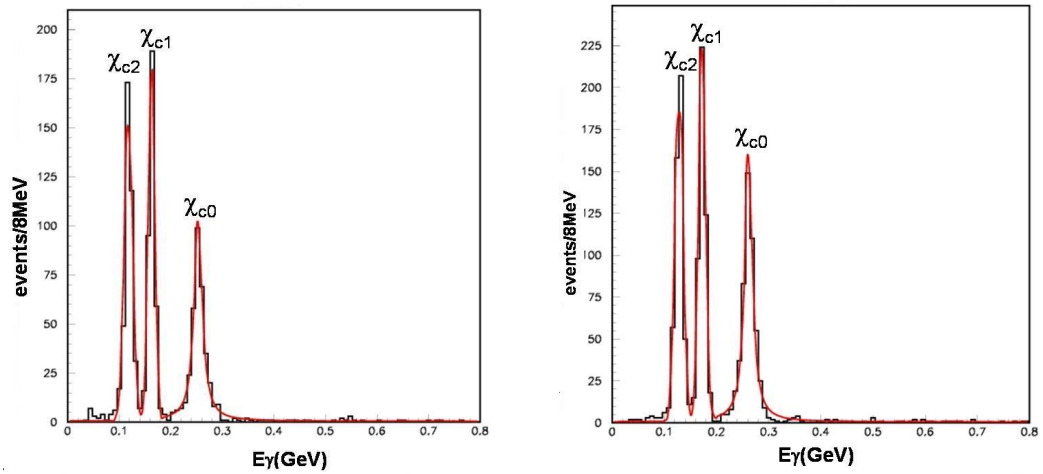

(a) $\chi_c \to \omega\omega$ sample for CLEO III MC (b) $\chi_c \to \omega\omega$ sample for CLEO-c MC

Figure 4–6: $\chi_c \to \omega\omega$ MC sample

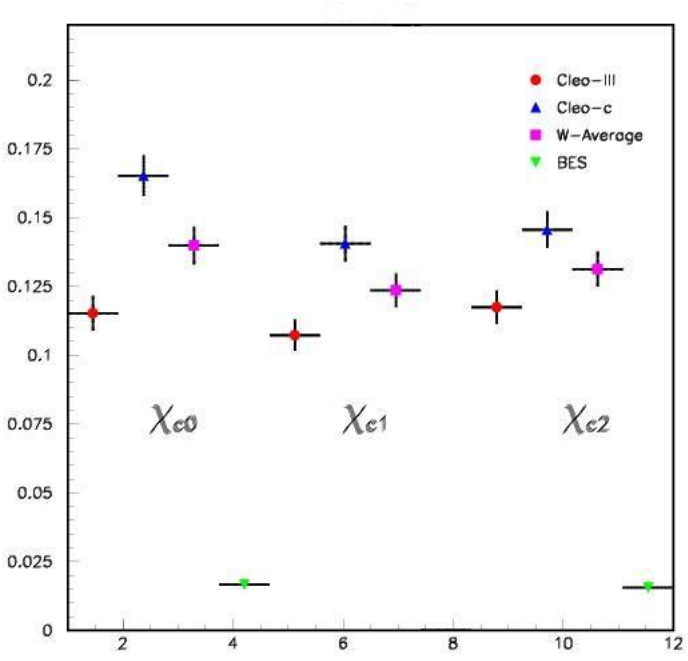

Figure 4–7: $\chi_c \to \omega\omega$ Efficiencies

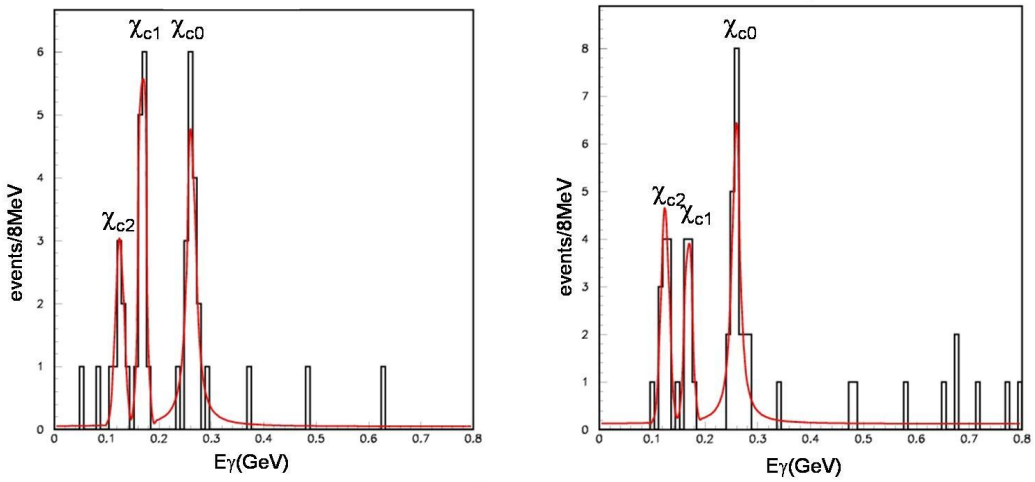

(a) $\chi_c \to \omega\omega$ sample for CLEO III data (b) $\chi_c \to \omega\omega$ sample for CLEO-c data

Figure 4–8: $\chi_c \to \omega\omega$ Data sample

Results

The number of observed data events (and the statistical errors) in CLEO III and CLEO-c (shown in Table 4–7) were measured by fitting the photon spectrum (Figures 4–8(a) and 4–8(b)) with the same functions used for the MC data. Again, our experimental resolution made it possible to separate the χ_{c1} and χ_{c2} peaks.

Table 4–7: Number of $\chi_c \to \omega\omega$ Events

Quantity	$\chi_{c0} \to \omega\omega$	$\chi_{c1} \to \omega\omega$	$\chi_{c2} \to \omega\omega$
CLEO III	19.9±4.8	13.9±3.8	9.7±3.2
CLEO-c	21.5 ± 4.9	8.6±3.1	10.9±4.9

Verification was done to check that the $\pi^+\pi^-\pi^{\mathbf{0}}$ combinations were consistent with the ω mass, as can be observed in Figures 4–9(a) and 4–9(b) (both CLEO III and CLEO-c are taken into account). Figure 4–9(a) shows $\pi^+\pi^-\pi^{\mathbf{0}}$ combinations that survive all cuts. The box in 4–9(b) represents a 50 MeV boundary around the nominal mass of ω(782 MeV), only events in side the box were considered.

In this case, branching ratios are determined by the following formula

$$BR(\chi_c \to \omega\omega) = \frac{N^{rec}_{\chi_c}}{N_{\psi(2S)} \cdot \epsilon} \cdot \frac{1}{BR(\psi(2S) \to \gamma\chi_c) \cdot BR(\omega \to \pi^+\pi^-\pi^{\mathbf{0}})^2 \cdot BR(\pi^{\mathbf{0}} \to \gamma\gamma)^2} \tag{4.6}$$

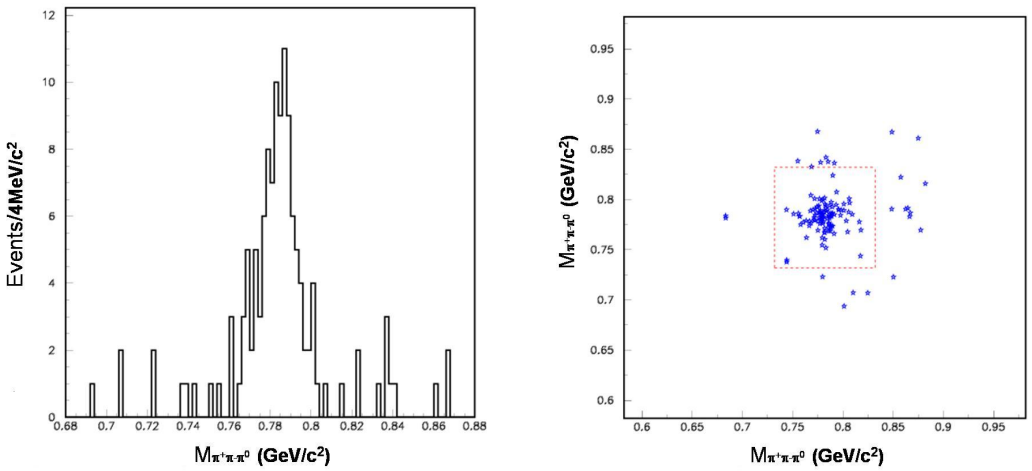

(a) $\pi^+\pi^-\pi^{\mathbf{0}}$ invariant mass (b) $\pi^+\pi^-\pi^{\mathbf{0}}$ vs $\pi^+\pi^-\pi^{\mathbf{0}}$ invariant mass scatter plot

Figure 4–9: $\pi^+\pi^-\pi^{\mathbf{0}}$ combinations

where:

$N_{\chi_c}^{rec}$ is the number of reconstructed χ_c events.

$N_{\psi(2S)}$ is the number of produced $\psi(2S)$ events recorded used in this analysis.

ϵ is the reconstruction efficiency for the χ_c decay mode.

BR($\psi(2S) \to \gamma\chi_c$) is the branching ratio for $\psi(2S) \to \gamma\chi_c$ decay taken from recent CLEO results [14].

BR($\omega \to \pi^+\pi^-\pi^{\mathbf{0}}$)is the branching ratio for $\omega \to \pi^+\pi^-\pi^{\mathbf{0}}$ decay taken from PDG [13].

BR($\pi^{\mathbf{0}} \to \gamma\gamma$) is the branching ratio for $\pi^{\mathbf{0}} \to \gamma\gamma$ decay taken from PDG [13].

Table 4–8 shows a summary of the final branching ratios, number of event and efficiencies for this mode. The first errors are statistical and the second are systematic.

systematics

Fit systematics were done in the same way as $\chi_c \to \phi\phi$, by varying the fit and taking those similar systematics to other data analysis of the experiment.

Table 4–8: $\chi_c \to \omega\omega$ Branching ratios and relevant numbers

Quantity	$\chi_{c0} \to \omega\omega$	$\chi_{c1} \to \omega\omega$	$\chi_{c2} \to \omega\omega$
Number of Events	41.3±9.7	22.6±6.9	20.5±6.7
Efficiency (%)	14.0±0.7	12.4±0.6	13.1±0.6
BR($\chi_c \to \omega\omega$)($\times 10^{-3}$)	1.38± 0.33± 0.10	0.89 ± 0.27± 0.10	1.03 ± 0.23± 0.16

In this particular analysis, the $\pi^{\mathbf{0}}$ reconstruction efficiencies systematic errors are also considered and were taken from previous analysis [11].

Our central value for each χ_c state is shown in the first point in figures 4–10(a), 4–10(b) and 4–10(c). The stability of this measurement is also remarkable.

Table 4–9 summarizes all contributions to systematic errors.The total systematic error is determined by the quadratic sum of all terms.

Table 4–9: $\chi_c \to \omega\omega$ Individual sources and total systematic error (%)

Source	$\chi_{c0} \to \omega\omega$	$\chi_{c1} \to \omega\omega$	$\chi_{c2} \to \omega\omega$
Number of $\psi(2S)$ Events	3	3	3
Luminosity	1	1	1
Using 3 Gaussians	2.3	0.4	0.3
Loosing χ^2	0.4	7.9	13.4
Reducing bin size in half	0.3	0.1	0.6
Changing fit range	0.6	0.0	0.2
Four Tracks	1.6	1.6	1.6
Two $\pi^{\mathbf{0}}$'s	1.5	1.5	1.5
BR($\psi(2S) \to \gamma\chi_{cJ}$ $(J = 0, 1, 2)$)	5.0	6.0	6.5
BR($\omega \to \pi^+\pi^-\pi^{\mathbf{0}}$)	0.9	0.9	0.9
Total	6.8	10.7	15.5

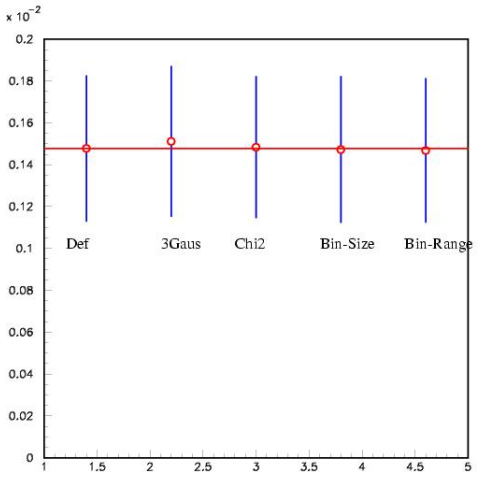

(a) $\chi_{c0} \to \omega\omega$ systematics

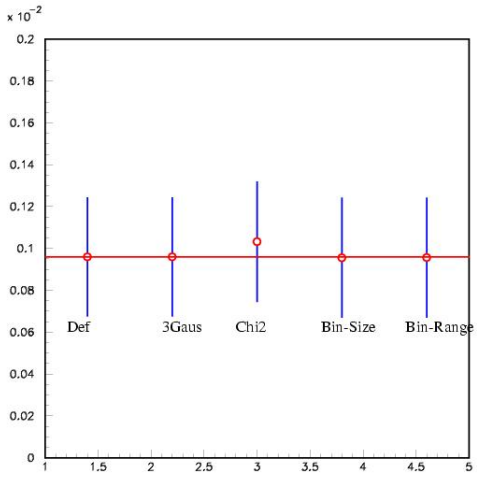

(b) $\chi_{c1} \to \omega\omega$ systematics

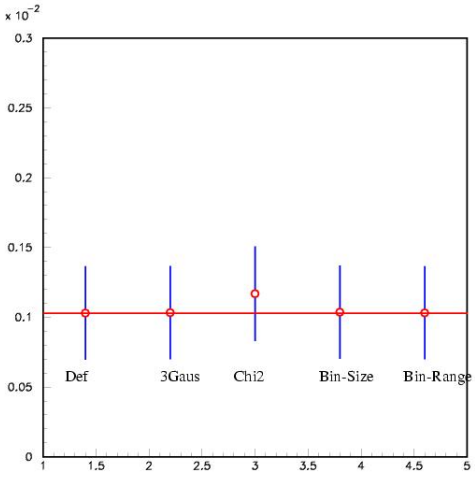

(c) $\chi_{c2} \to \omega\omega$ systematics

Figure 4–10: $\chi_c \to \omega\omega$ systematics

CHAPTER 5
CONCLUSIONS

In summary, we have measured the absolute branching ratios for the χ_c decaying into a pair of light vector mesons; $\omega\omega$ and $\phi\phi$. We have found the following results:

$$B(\chi_{c0} \to \omega\omega) = (\ 1.38 \pm 0.33 \pm 0.10)\ \times 10^{-3}$$

$$B(\chi_{c1} \to \omega\omega) = (\ 0.89 \pm 0.27 \pm 0.10)\ \times 10^{-3}$$

$$B(\chi_{c2} \to \omega\omega) = (\ 1.03 \pm 0.23 \pm 0.16)\ \times 10^{-3}$$

$$B(\chi_{c0} \to \phi\phi) = (\ 1.10 \pm 0.29 \pm 0.10)\ \times 10^{-3}$$

$$B(\chi_{c1} \to \phi\phi) = (\ 0.55 \pm 0.21 \pm 0.08)\ \times 10^{-3}$$

$$B(\chi_{c2} \to \phi\phi) = (\ 1.40 \pm 0.33 \pm 0.23\ )\ \times 10^{-3}$$

The precision on these measurements has been improved with respect to previous works done by BES as can be seen by comparing Tables 4–8 and 4–4 with Tables 2–1 and 2–2. Our measurement have smaller statistical and systematic error.

In addition, we are reporting branching ratios for $\chi_{c1} \to \omega\omega$ and $\chi_{c1} \to \phi\phi$ which are measured for the first time, showing that χ_{c1} can also decay in a pair of vector mesons.

Comparing Table 4–8 and 2–1 we can see that the sum of the $\chi_{c1} \to \omega\omega$ and $\chi_{c2} \to \omega\omega$ branching ratios obtained in this analysis matches with the branching ratio that BES [5] reports for $\chi_{c2} \to \omega\omega$, showing that they have both states (χ_{c1} and χ_{c2}) included in the $\chi_{c2} \to \omega\omega$ peak (see Fig. 2–2(a)) due to the fact that their resolution is not able to resolve these resonances. Our experimental resolution allows us to separate the two states which are only 46 MeV away.

These measurements, including the new χ_{c1} results, will help the actual theoretical work on glueball dynamics in progress [4].

The CLEO-c experiment plans to collect 30 million more $\psi(2S)$ by the end of summer 2006, when we plan to continue working on this subject by studying similar two vector decays for χ_c, such as $\chi_c \to K^{0*}\overline{K^{0*}}$ (which has been already started, see Appendix A) and $\chi_c \to \omega\phi$ which will be of fundamental interest for theoretical predictions on $\chi_c \to VV$ decays [4]. Due to the lack of statistics we were not able to study in more detail these modes. However, we expect to have a similar precision as for the other modes.

APPENDICES

APPENDIX A
$\chi_c \rightarrow K^{0*}\overline{K^{0*}}$

In a later stage of our work, we started working with another similar channel for $\chi_c \rightarrow VV$ as a compliment to our initial goal. It is the $\chi_c \rightarrow K^{0*}\overline{K^{0*}}$ decay mode:

$$\psi(2S) \rightarrow \gamma\chi_{cJ}\ (J = 0, 1, 2) \rightarrow \gamma K^{0*}\overline{K^{0*}} \rightarrow \gamma K^{+}\pi^{-}K^{-}\pi^{+} \tag{A.1}$$

The $\chi_c \rightarrow K^{0*}\overline{K^{0*}}$ decay unlike the $\chi_c \rightarrow \omega\omega$ and $\chi_c \rightarrow \phi\phi$ modes differs in the fact that this one doesn't decay into a pair of the same vector meson but a vector meson K^{0*} and its antiparticle $\overline{K^{0*}}$.

The analyisis began in a similar fashion as $\chi_c \rightarrow \omega\omega$ and $\chi_c \rightarrow \phi\phi$ using the same data for CLEO-c and CLEO III and generating 10000 MC events for CLEO III and 10000 for CLEO-c.

Event selection was done almost the same way as $\chi_c \rightarrow \phi\phi$ with the only difference that here the $K\pi$ combinations were required to be consistent with the K^{0*} mass within $\pm$ 100 MeV due to the fact that the K^{0*} has a large natural width.

The Maximum Likelihood method is used to fit the photon energy spectrum shown in Figures A–1(a), A–1(b) and the number of MC reconstructed signal events were measured to calculate the reconstruction eficciencies for CLEO III and CLEO-c (Table A–1).

In the process of verifying the kπ candidates, a difficulty appeared. The data sample seemed to have not just kπ combinations near the K^{0*} mass but a visible

Table A–1: $\chi_c \to K^{0*}\overline{K^{0*}}$ Efficiencies (%)

Quantity	$\chi_{c0} \to K^{0*}\overline{K^{0*}}$	$\chi_{c1} \to K^{0*}\overline{K^{0*}}$	$\chi_{c2} \to K^{0*}\overline{K^{0*}}$
CLEO III	33.7±1.0	29.0±1.0	30.5±1.0
CLEO-c	38.2±1.1	34.8±1.0	34.8±1.0

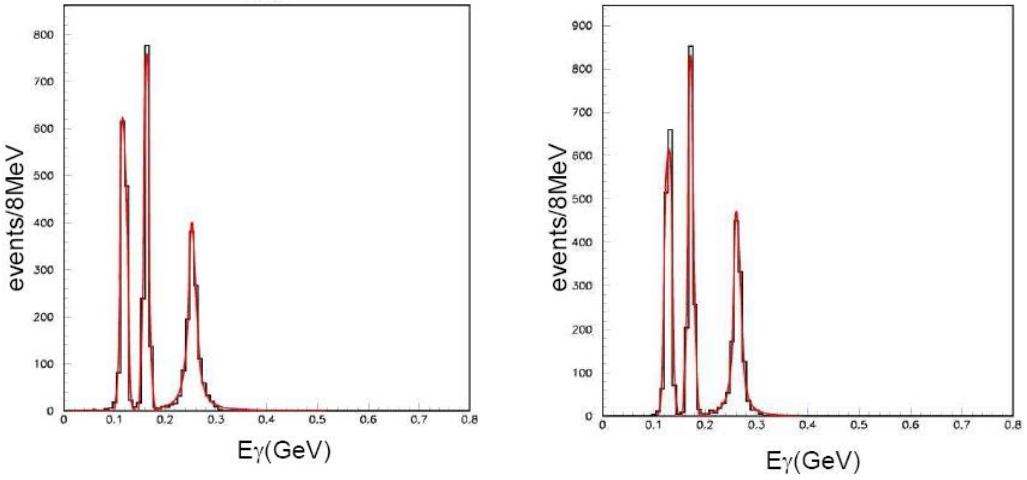

(a) $\chi_c \to K^{0*}\overline{K^{0*}}$ signal for CLEO III MC (b) $\chi_c \to K^{0*}\overline{K^{0*}}$ signal for CLEO III MC

Figure A–1: MC measured signals for $\chi_c \to K^{0*}\overline{K^{0*}}$

contamination from other K^* states. This can be seen in Figure A–2(c). The box in 4–4(b) represents a 100 MeV boundary around the nominal mass of K^{0*}(892 MeV). It is observable that the events are very scattered and there is no clear division between our candidates and the other states.

After this, we studied the contamination by plotting the events inside the acceptance region (inside the 100 MeV boundary), and at the sidebands. Figure A–2(a) shows the events inside the acceptance region and figure A–2(b) shows event outside the acceptance region (sidebands). It is observable that the signal on the sidebands is not negligible.

It can be seen that beside $\chi_c \to K^{0*}\overline{K^{0*}}$ there might be other $\chi_c \to KK\pi\pi$ resonances involved Possibly these states might be $K_2^*(1430)^0$ $\overline{K}_2^*(1430)^0$, $K_0^*(1430)^0$ $\overline{K}_0^*(1430)^0$ and/or $K_1^*(1270)$ $\overline{K}$.

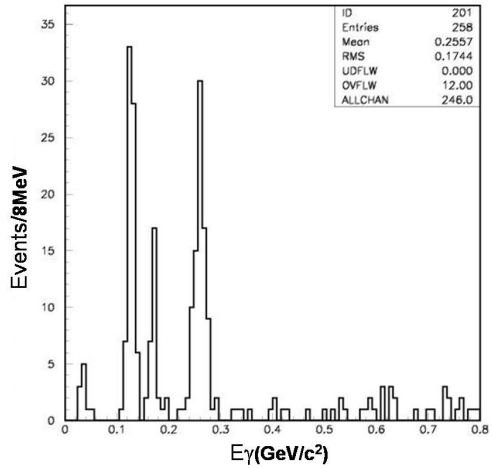

(a) $E\gamma$ inside acceptance region

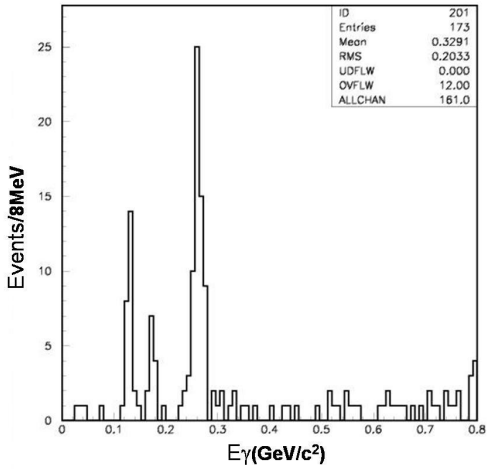

(b) $E\gamma$ on sidebands

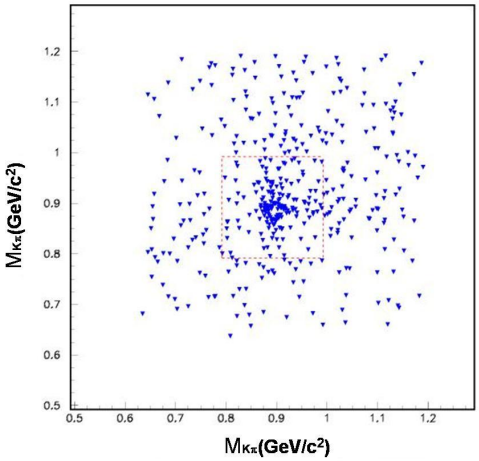

(c) K^* 1 vs K^* 2 mass scatterplot

Figure A–2: $\chi_c \to K^{0*}\overline{K^{0*}}$ sideband study

With the present amount of CLEO data, it is difficult at this moment to disintangle the other contributions. Further work is necessary to classify sidebands on $\chi_c \to K^{0*}\overline{K^{0*}}$. The experiment plans to take 30 million $\psi(2S)$ by the end of 2006 summer where we plan to continue working on this particular mode which will be fundamental for theoretical predictions on $\chi_c \to VV$ decays and glueball dynamics [4].

REFERENCE LIST

[1] S. M. McGee. A search for $\mathbf{D^0}$ - $\bar{D^0}$ mixing in the semileptonic decay of $\mathbf{D^0}$ $\rightarrow$ k$^*e\nu$. *Ph.D. Thesis, Wayne State University*, 2002.

[2] D. C. Cheng. *Elementary Particle Physics: An Introduction*. Addison-Wesley, 1979.

[3] J.P. Lansberg. J/ ψ , ψ' and υ production at hadron colliders, a review. *arXiv:hep-ph/0602091*, 2006.

[4] Q. Zhao. A coherent study of $\chi_c \rightarrow VV$, pp and ss. *arXiv:hep-ph/hep-ph/0508086*, 2005.

[5] M.Ablikim *et al.* (BES Collaboration). Observation of $\chi_c \rightarrow \omega\omega$ decays. *arXiv:hep-ph/hep-ph/0506045 Published on: Phys. Lett. B630: 7-13*, 2005.

[6] BES Collaboration. Study of the hadronic decays of χ_c states. *PHYS. REV D 60, 072001*, 1999.

[7] Cornell University Laboratory for Elementary Particle Physics. The `CESR` storage ring. *www.lns.cornell.edu/public/lab-info/cesr.html*.

[8] P. Zweber. Precision measurements of the timelike electromagnetic form factors of the pion, kaon, and proton. *Ph.D. thesis, Northwestern University*, 2006.

[9] M. Artuso *et al. Nucl. Instrum. Meth.* ***A441****, 374*, 2002.

[10] CLEO-c Collaboration. *A New Frontier of Weak an Strong Interactions*. CLNS 01/1742. Internal Document (yellow book), 2001.

[11] H. Mahlke and B. Heltsey. Branching fractions for $\psi(2S)$ transitions to J/ψ and for $J/\psi \rightarrow l^+l^-$. *CBX 04-47*, CLEO Internal Document, 2005.

[12] R. Brun *et al.* Computer code geant 3.21. *CERN Report No. W5013*, (unpublished), 1993.

[13] Particle Physics Group S. Eidelman *et al. Phys lett.* ***B592*** *, 814-835*, 2004.

[14] S. B. Athar *et al.* Cleo Colaboration. *Phys Rev.* ***D70****, 112002*, 2004.

BIOGRAPHICAL SKETCH

OSVALDO AQUINES

Osvaldo Aquines was born on Sept,1,1975, in Monterrey, Nuevo Leon, Mexico. In 1995 Osvaldo entered college at Tecnologico de Monterrey at Monterrey. Several years later, he graduated as Physical Engineer. In 2000 Just after graduating from College, he went to Mazatlan Sinaloa, to teach. He returned after that, in 2001, to his hometown to study for his MS in Statistics in the same institution he attended earlier. In 2003 he finished the MS and went to Puebla to teach again. There, he met Enrique Montiel, an Graduate of the University of Puerto Rico who encouraged him to come back to the field of physics, and so in August 2004, he started his studies towards a Master's in High Energy Physics.